Hindawi
International Transactions on Electrical Energy Systems
Volume 2022, Article ID 2330683, 20 pages
https://doi.org/10.1155/2022/2330683

Research Article

Stability Analysis of the Dual Half-Bridge Series Resonant Inverter-Fed Induction Cooking Load Based on Floquet Theory

Belqasem Aljafari,[1] **Pradeep Vishnuram**,[2] **Sureshkumar Alagarsamy**,[2] **and Hassan Haes Alhelou**[3]

[1]*Electrical Engineering Department, College of Engineering, Najran University, Najran 11001, Saudi Arabia*
[2]*Department of Electrical and Electronics Engineering, SRM Institute of Science and Technology, Chennai 603203, India*
[3]*Department of Electrical Power Engineering, Faculty of Mechanical and Electrical Engineering, Tishreen University, Lattakia 2230, Syria*

Correspondence should be addressed to Hassan Haes Alhelou; h.haesalhelou@gmail.com

Received 25 May 2022; Accepted 25 July 2022; Published 15 September 2022

Academic Editor: Bamidele Victor Ayodele

Induction heating (IH) applications aided power electronic control and becomes most attractive in recent years. Power control plays a vital role in any IH applications in which the stability of the converter is still a research hot spot due to variable frequency operation. In the proposed work, the stability of the converter is carried out based on the Floquet theory for dual-frequency half-bridge series inverter-fed multiload IH system. The dynamic behaviour of the converter is analyzed by developing a small-signal model of the converter. The system with a dynamic closed-loop controller results in poles and zeros lying outside the unit circle, which has poor closed-loop stability and up-down glitches in the frequency response plot. Hence, a proportional-integral (PI) compensator is used to mitigate the said issue, which results in a better response when compared with the open system and works satisfactorily. However, the system becomes unstable when the frequency is varied and the system also possesses a poor time domain response. Hence, the values of the controller gain are optimized with the Floquet theory, which is based on the Eigenvalues of the time domain model. For the optimized gains, the system possesses better stability for the variations in the switching frequency (20 kHz to 24 kHz), and also, the frequency response of the system is better with minimum time domain specifications. The performance of the system is simulated in MATLAB, and the response is noted for various switching frequencies in open loop, with a PI compensator, and with an optimized PI compensator. The output power is varied from 500 W to 18 W at load 1 and 250 W to 9 W at load 2. It is noted from the output response that the rise time is 0.0085 s, the peak time is 0.0001 s, and the peak overshoot is 0.1% with minimum steady-state error. Furthermore, the IH system is validated using a PIC16F877A microcontroller with the optimized PI controller, and the thermal image is recorded using a FLIR thermal imager.

1. Introduction

In recent years, induction heating (IH) has been widely used in several fields, which include medical, industrial, and domestic applications. It is a booming technology due to its meritorious advantages such as hygiene, indirect heat, noncontamination, zero pollution, and higher efficiency [1]. In the IH system, heat is produced on the workpiece due to the electromagnetic principle as it produces more eddy current on the surface of the material [2]. Hence, the rate of heat produced in the heating material depends on the switching frequency selection, which varies from 10 kHz to 1 MHz [3]. This high-frequency switching is achieved using the resonant inverter, which converts 50 Hz AC to high-frequency alternating current (HFAC) with a high power density and soft switching [4]. The selection of a specific converter for the application plays a vital role, in which a series half-bridge (HB) inverter is selected for the maximum power rating of up to 4.5 kW [5, 6]. The drawback of this topology is more switching stress across the switch [7]. In

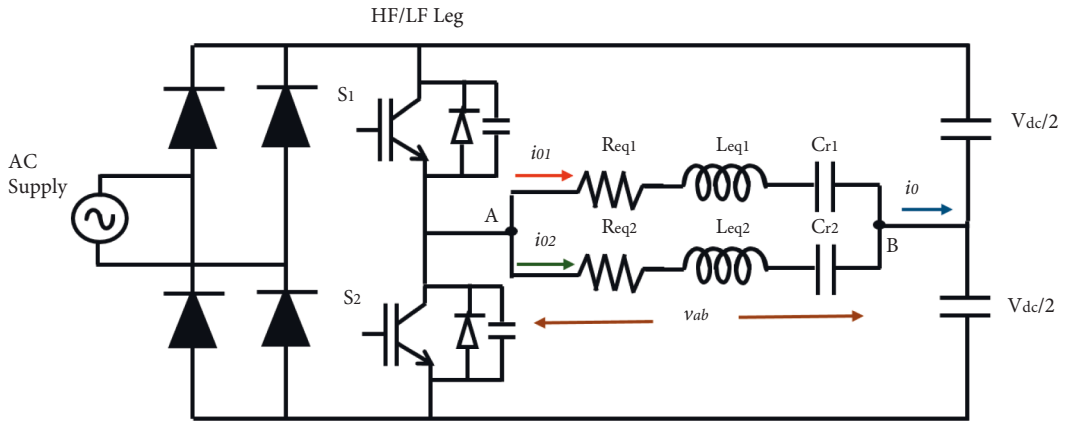

Figure 1: Circuit diagram of dual HB inverter.

[5], the switching stress is reduced using the auxiliary switched capacitor. However, the additional capacitor increases the passive elements and system time constants. This problem is overcome by using a full-bride (FB) inverter in which switching stress is shared by the four semiconductor switches. In addition, they can able to hold more power ratings, which are greater than 5000 W. In [8], a multifrequency FB series resonant inverter is developed into two loads. In the arrangement, the load frequency is selected twice the inverter frequency.

In recent years, a multioutput-based induction cooking scheme has been developed to feed power to many loads [9–13]. The converter topologies developed for feeding power include the modified HB and FB inverters. The novel topology is developed in [9], which includes HB and FB inverters, which are capable of performing the function of two FB inverters. The topology is connected to a single input and two loads with a common leg shared by both. The control algorithm is developed in such a manner that both the load can be controlled independently and simultaneously. In [10], a single-input multiple-load handling converter topology is developed. Power to the multiple loads is fed by the common HB inverter, and each load is controlled simultaneously by the inverter switches. The arrangement of the load is performed in such a manner that all are connected in parallel and independent power control is not feasible. A multioutput HB inverter feeding power to multiple loads is proposed in [11]. On this IH system, the HB inverter acts as the common inverter which converts DC into HFAC. Each load is connected with a series-connected single switch. Simultaneous power control is feasible with the switch.

Sharath Kumar et al. proposed a dual-frequency FB SRI to handle two loads. The output power is deployed using asymmetrical duty cycle (ADC) control in which simultaneous and independent power control is feasible. The proposed inverter consists of two legs, in which one leg takes care of the low frequency and the other one the high-frequency [12]. This control scheme results in the presence of DC components in the output voltage. This problem was overcome by Vishnuram and Ramachandiran [13]. HB inverter was used to feed power to two loads with two different frequencies. The output power is varied using pulse density modulation (PDM) control, in which simultaneous and independent control is feasible. A dual-frequency control is performed for the surface hardening of gear, which is a nonuniform shape [14].

Booma et al. developed the small-signal modelling of the HB inverter-fed IH system using the harmonics balance equation [15]. In this method, nonlinear variables in the state equations are expanded by the Taylor series and the transfer function for output voltage concerning duty cycle and frequency was obtained. The derived function was divided into the sum of cosine and sine terms with fixed frequency and variable duty cycle and with variable duty cycle and fixed frequency. The open-loop stability of the converter was analyzed for variations in duty cycle and frequency. Various researchers proposed the mathematical modelling of rotating and polar coordinate systems based on the traditional state plane method [16, 17]. However, these studies have not investigated the stability issues of the system with the resonant converters. In a small-signal model of a dual HB inverter with a common capacitor for multi-load cooking applications was proposed [18]. An open-loop Bode plot was obtained by providing the small perturbations in the switching frequencies and phase angle between voltage and current. The stability and controllability of a PLL-based IH system were proposed in [19]. The output power was controlled using the AVC control technique, and the power control margin was obtained using pole-zero plots. This method was time-consuming and does not depend on the qualitative analysis of the converter, which is very important for the stability analysis of the system. In addition, stability analysis was carried out in the frequency domain for a dual HB inverter-fed IH system, and a compensator was designed as per the obtained amplitude-phase and gain margin. The system was found to be stable in an open loop and failed in a closed loop. Therefore, it is necessary to obtain the closed-loop stability of the system under uncertain conditions. The stability of the periodic system is estimated by using the Floquet theory with the zero solution method [20]. This method uses the periodic solution of linear and nonlinear differential equations with

the different periodic solutions at the origin. The same has been used in PWM-controlled rectifiers, DC-DC converters, and inverters [21–23].

It is evident from the literature that, there is a quest in proposing the control algorithm to determine the closed stability of the system. In this paper, a methodology is presented using the Floquet theory to estimate the closed system stability for a wide range of load regulations. The small-signal modelling of the dual-frequency converter is obtained, and the stability analysis is determined by the Eigenvalue of the A matrix. The proposed system is validated and stability results are verified by simulation using Bode and polar plots, which provides an efficient scheme of dual-frequency inverter-fed IH system.

2. State-Space Modelling of Dual-Frequency Inverter

The circuit diagram of the dual HB inverter is illustrated in Figure 1. For the fixed frequency, the total resistance referred to the primary (coil) is represented as R_{eq1} and R_{eq2} and the total inductance referred to the primary (coil) is represented as L_{eq1} and L_{eq2}. The resonant capacitors are associated in series with equivalent resistance and inductance of each coil to form a series resonant tank. Modes of operation and switching frequency selection are briefed in [13]. A mathematical model of the system is essential to investigate system stability. Hence, v_{c1}, v_{c2}, i_{o1}, and i_{o2} are considered AC state variables. By approximating the state equations using the harmonic balance principle, state variables are resolved in terms of sine and cosine functions as i_{co1}, i_{so1}, v_{ccr1}, v_{scr1}, i_{co2}, i_{so2}, v_{ccr2}, v_{scr2}. The small-signal modeling of the dual-frequency HB inverter-fed induction cooking system is given as follows:

$$\frac{d\hat{i}_{s01}}{dt} = -\frac{\hat{v}_{scr1}}{L_{eq1}} - \frac{R_{eq1}}{L_{eq1}}\hat{i}_{s01} + \omega_{s1}\hat{i}_{c01} + I_{c01}\hat{\omega}_{s1} + \frac{2V_{in}}{L_{eq1}}\cos(2\pi\ D)\hat{d}, \tag{1}$$

$$\frac{d\hat{i}_{c01}}{dt} = -\frac{\hat{v}_{ccr1}}{L_{eq1}} - \frac{R_{eq1}}{L_{eq1}}\hat{i}_{c01} - \omega_{s1}\hat{i}_{s01} - I_{s01}\hat{\omega}_{s1} + \frac{2V_{in}}{L_{eq1}}\sin(2\pi\ D)\hat{d}, \tag{2}$$

$$\frac{d\hat{v}_{scr1}}{dt} = \frac{\hat{i}_{s01}}{C_{r1}} + \omega_{s1}\hat{v}_{ccr1} + V_{ccr1}\hat{\omega}_{s1}, \tag{3}$$

$$\frac{d\hat{v}_{ccr1}}{dt} = \frac{\hat{i}_{c01}}{C_{r1}} - \omega_{s1}\hat{v}_{scr1} - V_{scr1}\hat{\omega}_{s1}, \tag{4}$$

$$\frac{d\hat{i}_{s02}}{dt} = -\frac{\hat{v}_{scr2}}{L_{eq2}} - \frac{R_{eq2}}{L_{eq2}}\hat{i}_{s02} + \omega_{s2}\hat{i}_{c02} + I_{c02}\hat{\omega}_{s2} + \frac{2V_{in}}{L_{eq2}}\cos(2\pi\ D)\hat{d}, \tag{5}$$

$$\frac{d\hat{i}_{c02}}{dt} = -\frac{\hat{v}_{ccr2}}{L_{eq2}} - \frac{R_{eq2}}{L_{eq2}}\hat{i}_{c02} - \omega_{s2}\hat{i}_{s02} - I_{s02}\hat{\omega}_{s2} + \frac{2V_{in}}{L_{eq2}}\sin(2\pi\ D)\hat{d}, \tag{6}$$

$$\frac{d\hat{v}_{scr2}}{dt} = \frac{\hat{i}_{s02}}{C_{r2}} + \omega_{s2}\hat{v}_{ccr2} + V_{ccr2}\hat{\omega}_{s2}, \tag{7}$$

$$\frac{d\hat{v}_{ccr2}}{dt} = \frac{\hat{i}_{c02}}{C_{r2}} - \omega_{s2}\hat{v}_{scr2} - V_{scr2}\hat{\omega}_{s2}. \tag{8}$$

The state and output equation of the converter is

$$\dot{x} = Ax + B_1u_1 + B_2u_2, \tag{9}$$

$$y = Cx. \tag{10}$$

State variable matrix (x), inputs (u_1 and u_2), and output variable (y) are represented as

$$\begin{aligned} x &= \left[\hat{i}_{s01}\ \ \hat{i}_{c01}\ \ \hat{v}_{scr1}\ \ \hat{v}_{ccr1}\ \ \hat{i}_{s02}\ \ \hat{i}_{c02}\ \ \hat{v}_{scr2}\ \ \hat{v}_{ccr2}\right]^T, \\ u_1 &= \hat{d}, \\ u_2 &= \hat{\omega}_s, \\ y &= \hat{v}_0. \end{aligned} \tag{11}$$

The state matrix A is represented as

$$A = \begin{bmatrix} \frac{-R_{\text{eq1}}}{L_{\text{eq1}}} & \omega_{s1} & \frac{-1}{L_{\text{eq1}}} & 0 & 0 & 0 & 0 & 0 \\ -\omega_{s1} & \frac{-R_{\text{eq1}}}{L_{\text{eq1}}} & 0 & \frac{-1}{L_{\text{eq1}}} & 0 & 0 & 0 & 0 \\ \frac{1}{C_{r1}} & 0 & 0 & \omega_{s1} & 0 & 0 & 0 & 0 \\ 0 & \frac{1}{C_{r1}} & -\omega_{s1} & 0 & 0 & 0 & 0 & 0 \\ 0 & 0 & 0 & 0 & \frac{-R_{\text{eq2}}}{L_{\text{eq2}}} & \omega_{s2} & \frac{-1}{L_{\text{eq2}}} & 0 \\ 0 & 0 & 0 & 0 & -\omega_{s1} & \frac{-R_{eq2}}{L_{eq2}} & 0 & \frac{-1}{L_{\text{eq2}}} \\ 0 & 0 & 0 & 0 & \frac{1}{C_{r2}} & 0 & 0 & \omega_{s2} \\ 0 & 0 & 0 & 0 & 0 & \frac{1}{C_{r2}} & -\omega_{s2} & 0 \end{bmatrix}. \tag{12}$$

Input matrixes B_1 and B_2 are represented as

Table 1: Design specifications of dual half-bridge inverter.

Parameters	Values
V_{in}	50 V (DC)
P_{01}	500–1000 W
$R_{eq1} = R_{eq2}$	11 Ω
C_{r1}	620 nF
f_{r1}	18.5 kHz
f_{r2}	75 kHz
k_p	0.001
T_s	0.67 μs
D	50%
P_{02}	200–500 W
$L_{eq1} = L_{eq2}$	0.12 mH
C_{r2}	38 nF
f_{s1}	20 kHz
f_{s2}	80 kHz
k_i	7.526

$$B_1 = \begin{bmatrix} \frac{2V_{in}}{L_{eq1}}\cos(2\pi D) \\ \frac{2V_{in}}{L_{eq1}}\sin(2\pi D) \\ 0 \\ 0 \\ \frac{2V_{in}}{L_{eq2}}\cos(2\pi D) \\ \frac{2V_{in}}{L_{eq2}}\sin(2\pi D) \\ 0 \\ 0 \end{bmatrix}, \quad (13)$$

$$B_2 = \begin{bmatrix} I_{c01} \\ -I_{s01} \\ V_{ccr1} \\ -V_{scr1} \\ I_{c02} \\ -I_{s02} \\ V_{ccr2} \\ -V_{scr2} \end{bmatrix}.$$

Output matrix is represented as

$$C = \begin{bmatrix} R_{eq1} & R_{eq1} & 0 & 0 & R_{eq2} & R_{eq2} & 0 & 0 \end{bmatrix}, \quad (14)$$

where

$$I_{s01} = \frac{V_{in}\omega_{s1}^2 C_{r1}{}^2 R_{eq1}}{\lambda_1},$$

$$I_{c01} = \frac{V_{in}\omega_{s1}C_{r1}\left(1-\omega_{s1}^2 L_{eq1}C_{r1}\right)}{\lambda_1},$$

$$V_{ccr1} = \frac{V_{in}\left(1-\omega_{s1}^2 L_{eq1}C_{r1}\right)}{\lambda_1},$$

$$V_{scr1} = \frac{V_{in}\omega_{s1}C_{r1}R_{eq1}}{\lambda_1},$$

$$\lambda_1 = \omega_{s1}^4 C_{r1}{}^2 L_{eq1}{}^2 - 2\omega_{s1}^2 C_{r1}L_{eq1} + 1 + \omega_{s1}^2 C_{r1}{}^2 R_{eq1}^2, \quad (15)$$

$$I_{s02} = \frac{V_{in}\omega_{s2}^2 C_{r2}{}^2 R_{eq2}}{\lambda_2},$$

$$I_{c02} = \frac{V_{in}\omega_{s2}C_{r2}\left(1-\omega_{s2}^2 L_{eq2}C_{r2}\right)}{\lambda_2},$$

$$V_{ccr2} = \frac{V_{in}\left(1-\omega_{s2}^2 L_{eq2}C_{r2}\right)}{\lambda_2},$$

$$V_{scr2} = \frac{V_{in}\omega_{s2}C_{r2}R_{eq2}}{\lambda_2}$$

$$\lambda_2 = \omega_{s2}^4 C_{r2}{}^2 L_{eq2}^2 - 2\omega_{s2}^2 C_{r2}L_{eq2} + 1 + \omega_{s2}^2 C_{r2}{}^2 R_{eq2}^2.$$

The perturbed output voltage of load 1 and 2 is

$$\begin{aligned} \hat{p}_{01} &= R_{eq1}\hat{i}_{s01}^2 + R_{eq1}\hat{i}_{c01}^2, \\ \hat{p}_{02} &= R_{eq2}\hat{i}_{s02}^2 + R_{eq2}\hat{i}_{c02}^2. \end{aligned} \quad (16)$$

The transfer function of output to duty cycle (G_{pd}) and output to switching frequency (G_{pf}) in the discrete domain with sampling time (T_s) is

$$\begin{aligned} G_{p\,d}(z) &= \frac{\hat{p}_0}{d} \\ &= C(zI - A)^{-1}\mathbf{B}_1 T_s, \end{aligned} \quad (17)$$

$$\begin{aligned} G_{pf}(z) &= \frac{2\pi\hat{p}_0}{\hat{\omega}_s} \\ &= 2\pi C(zI - A)^{-1}\mathbf{B}_2 T_s. \end{aligned} \quad (18)$$

This work focuses on the stability of the system for varying switching frequencies with a fixed duty cycle.

Table 2: Parameters of the converter and transfer function for each case.

Case	Frequency (kHz)	Z domain transfer function	Remarks
1	20	$\frac{0.21395(z-3.36)(z-0.5789)(z-0.08662)}{(z^2-0.2453z+0.08966)(z^2+0.6937z+0.9399)} / \frac{(z-0.7289)(z-0.5685)(z-0.1437)(z-0.1896)}{(z^2-0.23z+0.0825)(z^2+0.6503z+0.4875)}$	Poles inside the unit circle, zeros lie outside the unit circle, up-down and down-up glitches, multiple zero crossings
2	21	$\frac{-1.0639(z-2.4)(z-0.7276)(z+0.2778)(z+0.1674)}{(z-0.04194)(z^2+0.9781z+0.3445)} / \frac{(z-1.178)(z-0.7253)(z-0.1126)(z-0.0119)}{(z^2-0.5716z+0.08249)(z^2+1.044z+0.4799)}$	Poles and zeros lie outside the unit circle, up-down glitches, multiple zero crossing
3	22	$\frac{0.10256(z+20.32)(z+06576)(z+0.4438)}{(z^2-0.09238z+0.06223)(z^2+0.1188z+0.08069)} / \frac{(z-1.705)(z-0.008356)(z^2+1.297z+0.473)}{(z^2-0.1088z+0.08171)(z^2+0.1216z+0.08247)}$	Poles and zeros lie inside the unit circle, up-down glitches, multiple zero crossings
4	23	$\frac{0.10899(z+13.81)(z+06583)(z+0.4486)}{(z^2-0.4878z+0.06637)(z^2+0.4962z+0.08218)} / \frac{(z-2.296)(z-0.006288)(z^2-1.365z+0.4668)}{(z^2+0.5386z+0.08172)(z^2+0.4966z+0.08245)}$	Poles outside and zeros inside, up-down glitches, single zero crossing
5	24	$\frac{0.020908(z+46.86)(z^2+0.4962z+0.08218)}{(z^2-0.3221zz+0.07516)(z^2+0.9989z+0.3216)} / \frac{(z-2.296)(z-0.004993)(z^2-0.4273z+0.08243)}{(z^2+0.3217z+0.08174)(z^2+01.22z+0.461)}$	Poles outside and zeros inside, unit circle, up-down glitches

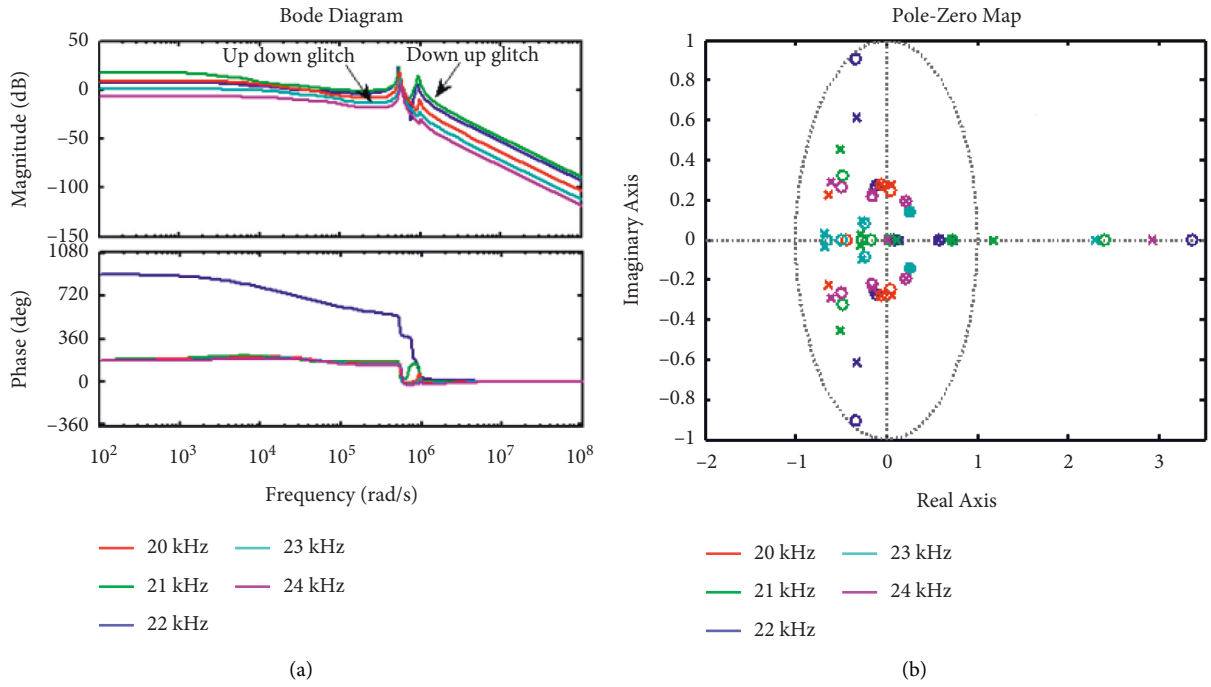

FIGURE 2: Frequency response of converter for different frequencies. (a) Bode diagram, (b) pole-zero map.

3. Analysis of the Dual-Frequency Half-Bridge Inverter-Fed IH Topology

In IH applications, frequency control plays an important role in varying the output power. When the frequency is deployed for real-time applications, the stability of the system needs to be investigated. In this section, frequency domain analysis of the developed IH system is described. Also, the stability of the system is investigated using the PI compensator and Floquet stability criterion.

3.1. Frequency Response of Dual-Frequency HB SRI-Fed IH System. The design of the dual HB SRI-fed IH system is validated using the frequency domain approach. The parameters for evaluating the proposed converter are listed in Table 1. The stability analysis of the IH converter topology is conceded out using pole and zero for the variation in switching frequency. In this work, the frequency of load 2 (f_2) is chosen as four times greater than load 1 (f_1). The capacitor is selected appropriately to make each load respond to its designed frequency (20 kHz for load 1 and 80 kHz for load 2) and it acts as a high impedance for other loads [13]. The stability of the system is investigated for the switching frequencies ranging from 20 kHz to 24 kHz.

The frequency response of the dual half-bridge SRI-fed IH system for various switching frequencies is presented, and an expression for variations in output voltage concerning frequency is given in Table 2. For stability analysis, the s-domain model of the system is converted into a discrete domain using the bilinear transformation method. The sampling time (t_s) is selected as $t_s \gg 1/(2 * \omega_{gc})$, where ω_{gc} is the gain cross-over frequency. The transient response for various f_s is shown in Figure 2, which demonstrates the necessity of improving the dynamic response of the system based on the poles and zeros for the variations in output voltage concerning the frequency. The frequency response using the Bode plot of the open-loop system is illustrated in Figure 2(a), and stability analysis using a pole-zero plot is shown in Figure 2(b), for 5 cases with different switching frequencies. In case 1, all poles lie inside the unit circle and zeros lie outside the unit circle. In the frequency response, there exist the up-down and down-up glitches with multiple zero crossings in the magnitude plot due to low damping of oscillations.

In case 2, poles and zeros lie outside the unit circle, which creates an instability problem. Also, in frequency response, there exist up-down glitches with multiple zero crossings in the magnitude due to the low damping oscillations. In case 3, the system is stable as poles and zeros lie inside the unit circle. However, there are up-down glitches and multiple zero crossings in the frequency response due to which the system becomes conditionally unstable. In case 4, poles lie outside the unit circle and zeros lie inside, which creates conditionally marginal stability in the system. There are also exist the up-down glitches in the frequency response with a single zero crossing in the magnitude plot. In case 5, it is confirmed from the pole-zero plot that poles lie outside the unit circle and zeros lie inside, creating the instability issue, and also there exist up-down glitches in the frequency response of the system. It is confirmed from the analysis that the system is stable only for a 20 kHz switching frequency, whereas there also exist multiple zero cross-over points in the magnitude of the frequency plot. This results in low

damping oscillations and stability issues. Hence, the design of a proper compensator is mandatory to overcome the said issue.

3.2. Compensator Design for Dual-Frequency HB SRI-Fed IH System. The closed-loop PI compensator is designed to supervise the system's stability for various switching frequencies. The block diagram of the closed-loop system with unity feedback ($H = 1$) is illustrated in Figure 3. The expression for the plant G_{Pd} is given in Equation (17). The gain of the VCO (G_{vco}) is fixed at 1000 and the expressions pertaining to the PI compensator are $G_{PI} = k_p + k_i/s$. The values of the proportional gain (k_p) = 0.001 and integral gain (k_i) = 7.526 are designed using the MATLAB SISO tool. The frequency response of the developed IH system is plotted for various values of the switching frequencies, and these are presented as various cases. The values of switching frequencies and the transfer function of the output power to the switching frequency for each case are expressed in Table 3. The frequency response of each case is shown in Figure 4 to illustrate the improvement in the performance of the system when compared with the open-loop study. The Bode diagram and pole-zero plot for various switching frequencies under different cases are illustrated in Figures 4(a) and 4(b), respectively. It is understood from the figures that, in case 1, poles and zeros lie away from the unit circle and there is an up-down glitch in the frequency response. In case 2, poles lie inside the unit circle and zeros lie outside the unit circle, which leads to a nonminimal phase in the system. Also, in frequency response, there exist the up-down and down-up glitches which result in high transients on the output side.

In case 3, the poles of the system lie on the unit circle and zeros lie inside the unit circle. Hence, the system is marginally stable, but there exists the up glitch, up-down, and down-up glitches in the frequency response, which result in the poor transient response of the system. In case 4, poles lie outside and zeros lie inside the unit circle, which leads to instability in the system, and also there existmultiple phase cross-over points with reduced glitches as compared with previous cases. In case 5, poles lie outside and zeros lie inside the unit circle, which results in a down-up glitch and multiple phase cross-over points in the frequency response of the system. This leads to instability issues and poor transient performance of the system. Though the performance of the designed system is satisfactory as compared with the open-loop system, it is necessary to optimize the values of controller gain to make the system stable with an improved dynamic response.

3.3. Optimizing k_p and k_i Using Floquet Stability Criterion. The Floquet theory is used to obtain the stability of the time domain periodic system. The state transition matrix (ϕ) of (9) and (10) is [24]

$$\varphi(t, t_0) = P(t)e^{Q(t-t_0)}P^{-1}(t_0), \tag{19}$$

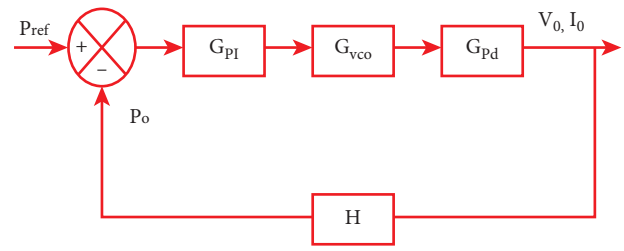

Figure 3: General block diagram of the closed-loop system with PI compensator.

where $P(t)$, Q, and t_0 represent the nonsingular periodic matrix, constant matrix, and arbitrary constant with zero as the initial value, respectively.

The DC operating point of the dual half-series resonant inverter is obtained with steady-state equations of the converter. It is found that, for any value of period T, condition $X(t) = X(t + T)$ is satisfied. Hence, the Floquet theorem can be applied to this system as it is periodic in nature. The expression pertaining to perturbation of duty cycle and switching frequency is given in Equations (1)–(8).

The condition for the system's stability is given by [25]

$$\lim_{n\longrightarrow\infty} = \left\|A^n\right\| = 0. \tag{20}$$

By the final value theorem, the system's stability is confined by the modulus of all eigenvalues of matrix A, which should be less than 1.

A and ϕ matrixes are constant for dual-frequency HB series resonance inverter, and Eigenvalues of the A matrix are obtained by $|\lambda I - A| = 0$. According to the Floquet theorem, a system is stable when the magnitude of the maximum value of the eigenvalue (λ_{max}) is less than one, i.e., $\lambda_{max} = \max |\text{eig (A)}| < 1$ for $T \neq 0$ and unstable for $\lambda_{max} > 1$. This relation helps in obtaining the stability of the dual-frequency converter for variations in output voltage with a fixed duty cycle.

The stability analysis of the dual half-bridge series resonant inverter is obtained by calculating the closed-loop transfer function of matrix A. The steady operating frequency is substituted as 20 kHz for load 1 and 80 kHz for load 2 in (18), and closed-loop controller gain is obtained as $k_p = 0.001$ and $k_i = 7.526$. According to the Floquet theorem, the system is stable for $\lambda_{max} < 1$. The stability of the system is investigated under two conditions as listed below:

Case 1.: In order to obtain the stability of the system, the value of k_p is fixed at 0.001 and k_i is varied from 6 to 14. An Eigenvalues plot for fixed k_p and varying k_i is shown in Figure 5. It is inferred from the plot that, for $k_i = 6$, the maximum value of eigenvalue is less than 1. Hence, according to the Floquet theory, the IH system is stable for $k_i \leq 6$.

Case 2.: Similarly, in order to estimate the k_p value, k_i is selected as 6 and k_p is varied from 0.003 to 0.0008. The respective plot is shown in Figure 6. It is understood

Table 3: Parameters of the converter and transfer function for each case with $k_p = 0.001$ and $k_i = 7.526$.

Case	Frequency (kHz)	Transfer function	Remarks
1	20	$\frac{-0.00054409(z-1.716)(z-0.9785)(z-0.578)}{(z-0.08503)(z^2-0.4584z+0.1942)(z^2-2.792z+2.209)} / \frac{(z-1)(z-1.059)(z-0.9291)(z-0.5766)(z-0.001522)}{(z^2-3.421z+3.056)(z^2-0.4423z+0.1808)}$	Poles, zero far away from the unit circle, up-down glitch
2	21	$\frac{-0.00053575(z-2.98)(z-0.9785)(z-0.7292)}{(z-0.03905)(z^2-1.118z+0.3233)(z^2-0.3049z+0.03889)} / \frac{(z-0.9646)(z-0.7329)(z-0.01836)(z^2+1.075z+0.2972)}{(z^2-0.289z+0.03816)(z^2-0.7794z+0.0385)}$	Poles inside zero outside, up-down and down-up glitches
3	22	$\frac{0.00012195(z+7.676)(z-0.9785)}{(z^2-0.08753z+0.06415)(z^2+0.1664z+0.07043)(z^2-0.1284z+0.1896)} / \frac{(z-0.7329)(z^2+1.964z+0.9842)(z^2+1.707z+0.0715)}{(z^2-0.1504z+0.1078)(z^2-0.08469z+0.213)}$	Poles on the unit circle zero inside, up glitch, up-down, and down-up glitches
4	23	$\frac{5.5486*10^{-5}(z+13.16)(z-0.9785)}{(z^2-0.4947z+0.06768)(z^2+0.4825z+0.07938)(z^2-0.8809z+0.2171)} / \frac{(z-1.84)(z-1.015)(z-0.01396)(z^2+0.4947z+0.06769)}{(z^2-0.4825z+0.07938)(z^2-0.08809z+0.2171)}$	Poles outside and zero inside, multiple phase cross-over point
5	24	$\frac{7.6821*10^{-7}(z+648.3)(z-0.9785)}{(z^2-0.955z+0.2443)(z^2+0.4258z+0.08126)(z^2-0.3234z+0.07547)} / \frac{(z-1.005)(z-1)(z-0.00788)(z^2+1.099z+0.3155)}{(z^2-0.4265z+0.08135)(z^2-0.3303z+0.08281)}$	Poles outside and inside the unit circle, multiple phase cross-over points

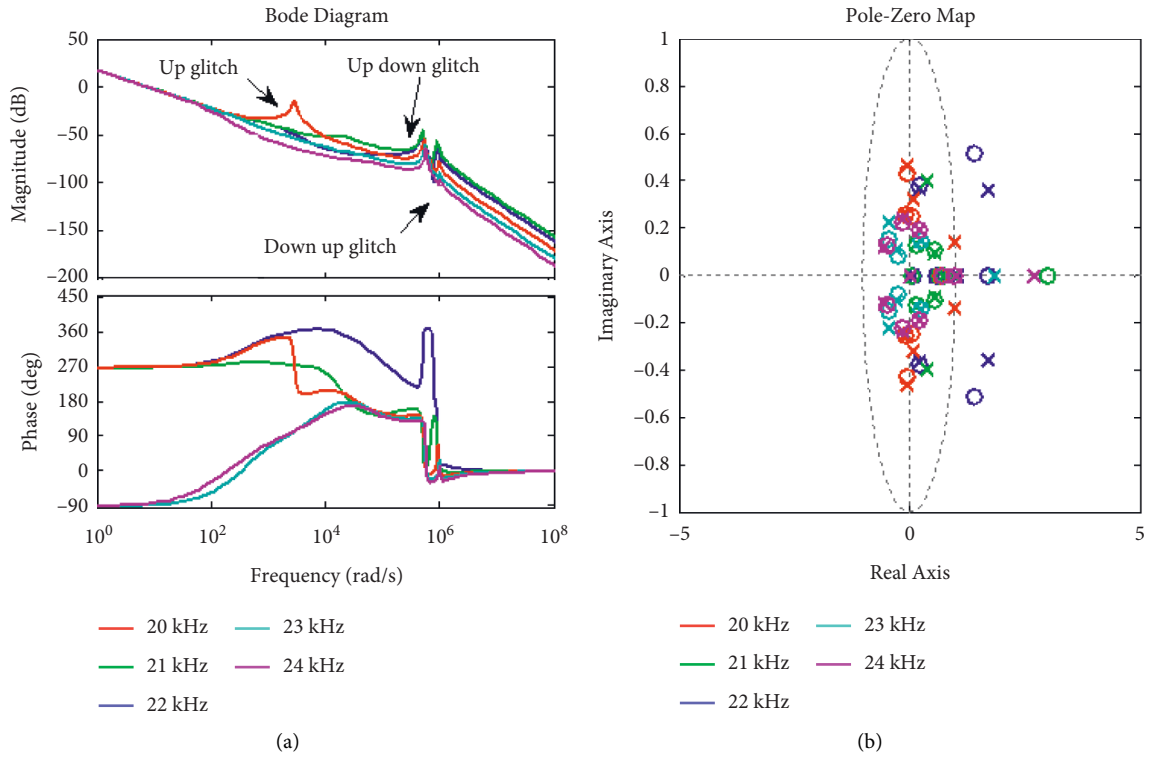

Figure 4: Compensated frequency response of the converter for different frequencies. (a) Bode diagram, (b) pole-zero map.

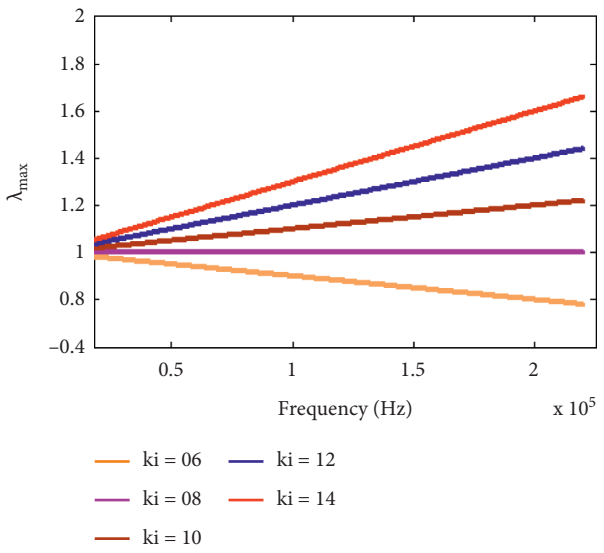

Figure 5: Eigenvalues plot for fixed k_p and varying k_i.

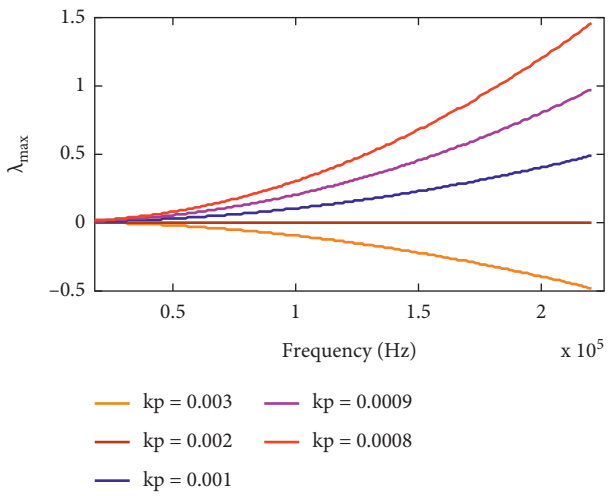

Figure 6: Eigen values plot for fixed k_i and varying k_p.

from the plot that the system is stable for $k_p \leq 0.003$, as the value of λ_{max} is greater than 1. Hence, for the stable operation of the system, the marginal values of k_p and k_i should be chosen to be greater than 0.003 and less than 6, respectively.

The frequency response of the converter for the optimized value of $k_p = 0.004$ and $k_i = 4$ is shown in Figure 7. It is inferred from the figure that, for all the five cases, the poles and zeros of the system lie inside the unit circle, which ensures the stability of the system. Also, up-down, down-up glitches are less in all five cases when compared with the compensated frequency response of the converter. The step response of the system with and without optimized values of k_p and k_i for 20 kHz, 22 kHz, and 24 kHz is shown in Figure 8. It is inferred from the response that the system has minimum peak overshoot, faster rise, and settling time for the optimized values of $k_p = 0.004$ and $k_i = 4$.

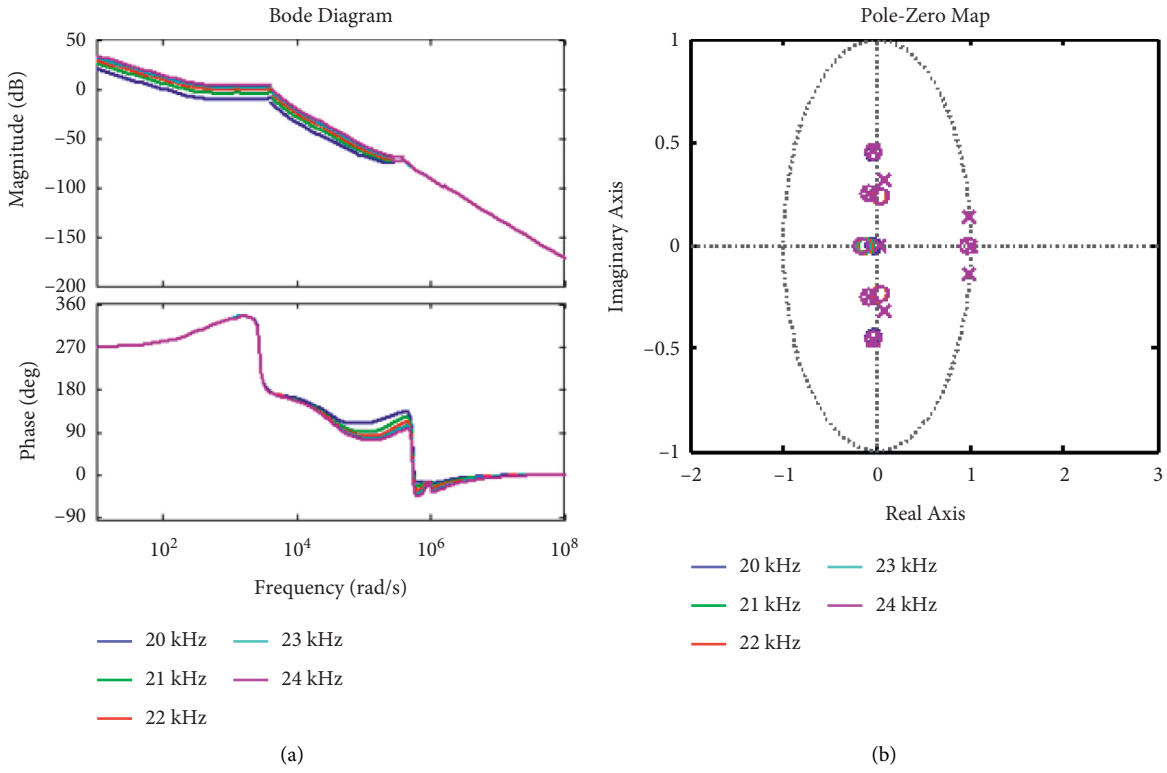

Figure 7: Frequency response of the converter for the optimized value of k_p and k_i. (a) Bode plot, (b) pole-zero map.

4. Simulation Results of the Developed System

Simulation of a dual HB SRI-fed IH system is carried out in MATLAB as per the listed specifications. The performance of the system is studied for different cases, as listed below.

4.1. Open-Loop Response of Dual-Frequency Half-Bridge SRI-Fed IH System. The dual half-bridge SRI is designed to operate with a 20 kHz switching frequency for load 1 and an 80 kHz switching frequency for load 2. The switching frequency ratio is maintained as 1 : 4 so that the capacitor values are chosen appropriately to make each load respond to its frequency and act as a higher impedance path for other frequencies. The power control is achieved by adjusting f_s from 20 kHz to 24 kHz for load 1 and four times greater for load 2. The main waveforms of load 1 and load 2 are illustrated in Figure 9. The output voltage and its expanded waveform are shown in Figures 9(a) and 9(b), respectively. It is inferred from the expanded view that the output voltage includes the superimposition of 20 kHz and 80 kHz output switching frequencies. The output current of load 1 with a 20 kHz switching frequency is illustrated in Figure 9(c), and its expanded view is shown in Figure 9(d). Similarly, the output current of load 2 with an 80 kHz switching frequency is shown in Figure 9(e), and its expanded view is shown in Figure 9(f). The selected capacitors allow 20 kHz current to flow through load 1 and 80 kHz current to flow through load 2 and act as open circuits for other frequencies. The output power waveform of load 1 and load 2 is demonstrated in Figure 9(f). It is inferred that the power dissipation of load 1 is 500 W and load 2 is 250 W at rated operating conditions. Due to the variation in the load impedance of the loads, the power dissipation is not uniform across the loads. It is inferred from Figure 9 that the open-loop system has a high peak overshoot due to the up-down glitches in the frequency response of the converter.

The output power is varied by adjusting the switching frequency of the inverter. In the open-loop study, the output response is noted for a 22 kHz switching frequency for load 1 and 88 kHz for load 2. The main waveform is illustrated in Figure 10. The output voltage waveform is shown in Figure 10(a). Output current of load 1 and load 2 is presented in Figures 10(b) and 10(c) respectively. The RMS value of output current is 4.26 A for load 1 and 3.02 A for load 2. At this switching frequency, there is a 40% decrease in the rated power. Hence, the output power is reduced from 500 W to 200 W in load 1 and 250 W to 100 W in load 2 as illustrated in Figure 10(d). Similarly, the main waveform for the 24 kHz switching frequency for load 1 and the 88 kHz switching frequency for load 2 is presented in Figure 11. The output voltage and current of load 1 and load 2 are shown in Figures 11(a)–11(c) respectively. The RMS value of the output current is 1.28 A for load 1 and 9 A for load 2. At this switching frequency, there is a reduction of 3.6% of the rated power. Hence, the output power is reduced from 500 W to 18 W in load 1 and 250 W to 9 W in load 2, as illustrated in Figure 11(d).

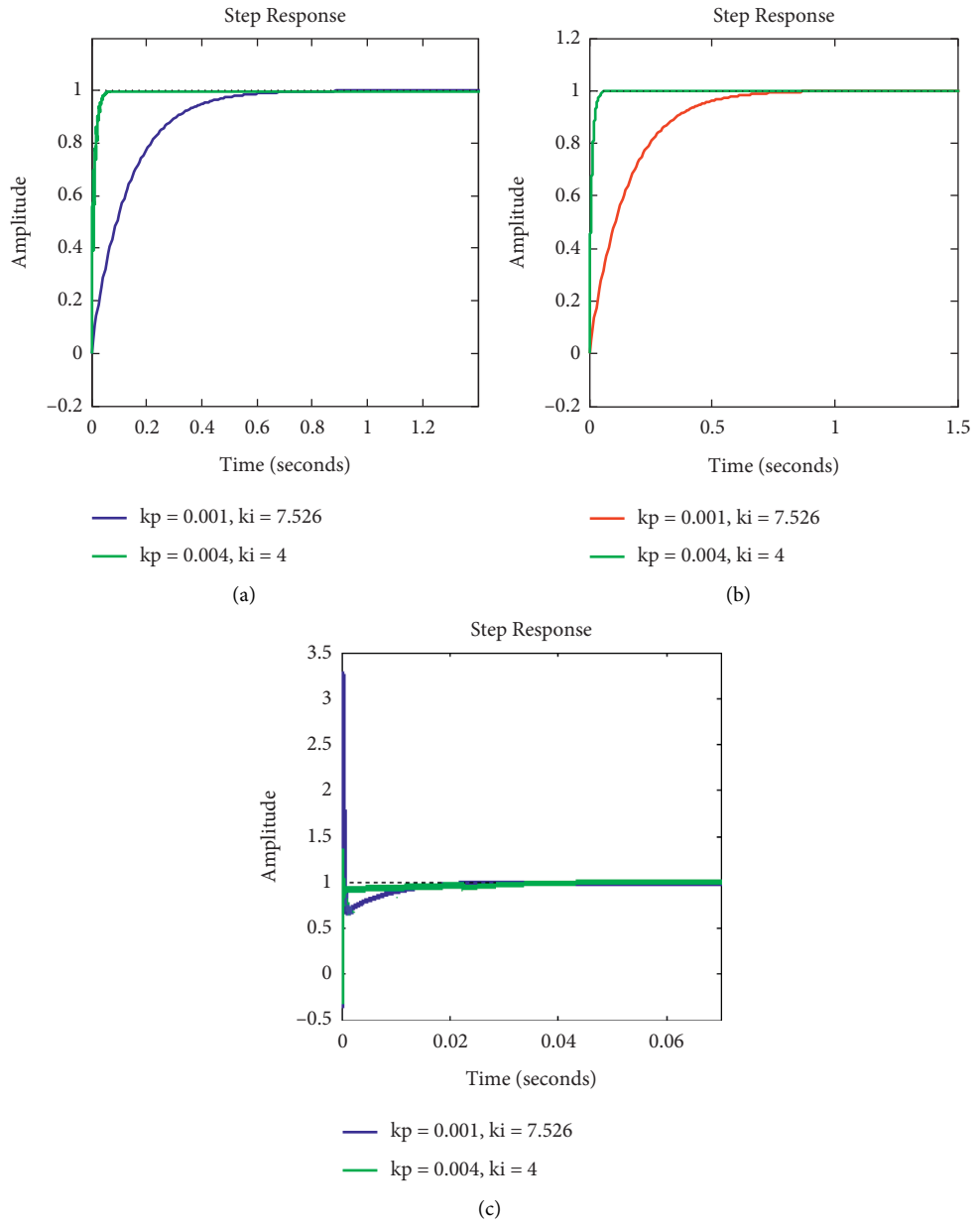

FIGURE 8: Step response of the system with and without optimized k_p and k_i values for the various switching frequencies: (a) 20 kHz, (b) 22 kHz, and (c) 24 kHz.

The computation of output power for various switching frequencies is given in Table 4, and the impact of output power on the switching frequency variations is presented in Figure 12. It is observed from the figure that the output power can be controlled from 100% to 3.6% of the rated power for the variation in switching frequency from 20 kHz to 24 kHz for load 1 and 80 kHz to 88 kHz for load 2.

4.2. Closed-Loop Response of SRI with PI Compensator. Power control plays a vital role in IH applications along with system stability. It is inferred from Figure 2 that the system is stable when operates at a 20 kHz switching frequency (close to resonant frequency) and for other switching frequencies, it is unstable. Hence, the PI compensator is designed to make the system stable, and the performance of the system is included in Table 3. The output response of the system for

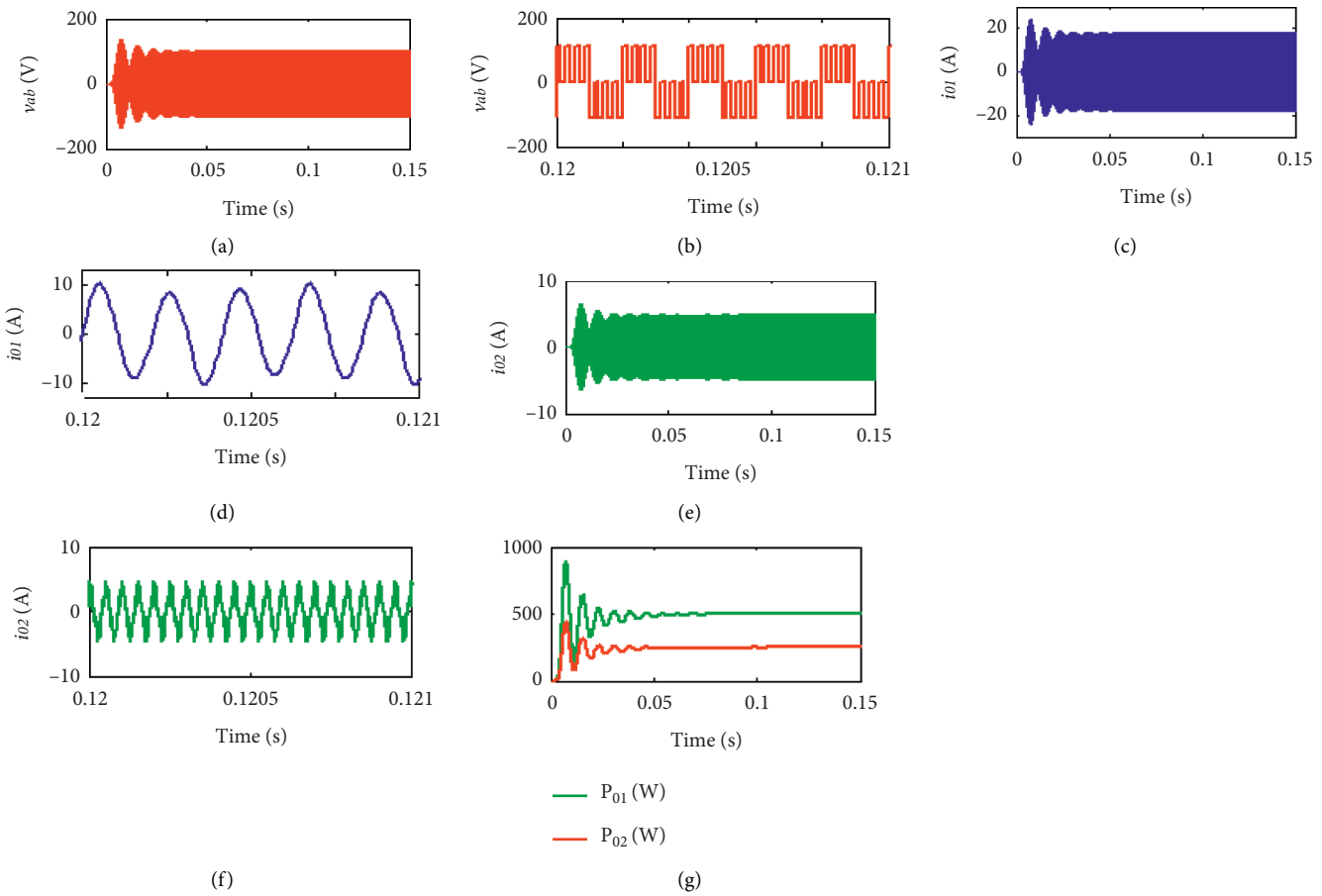

Figure 9: Main waveforms. (a) Output voltage, (b) expanded view of output voltage, (c) output current of load 1 with 20 kHz switching frequency, (d) expanded view of the output current of load 1, (e) output current of load 2 with 80 kHz switching frequency, (f) expanded view of the output current of load 2, and (g) output power.

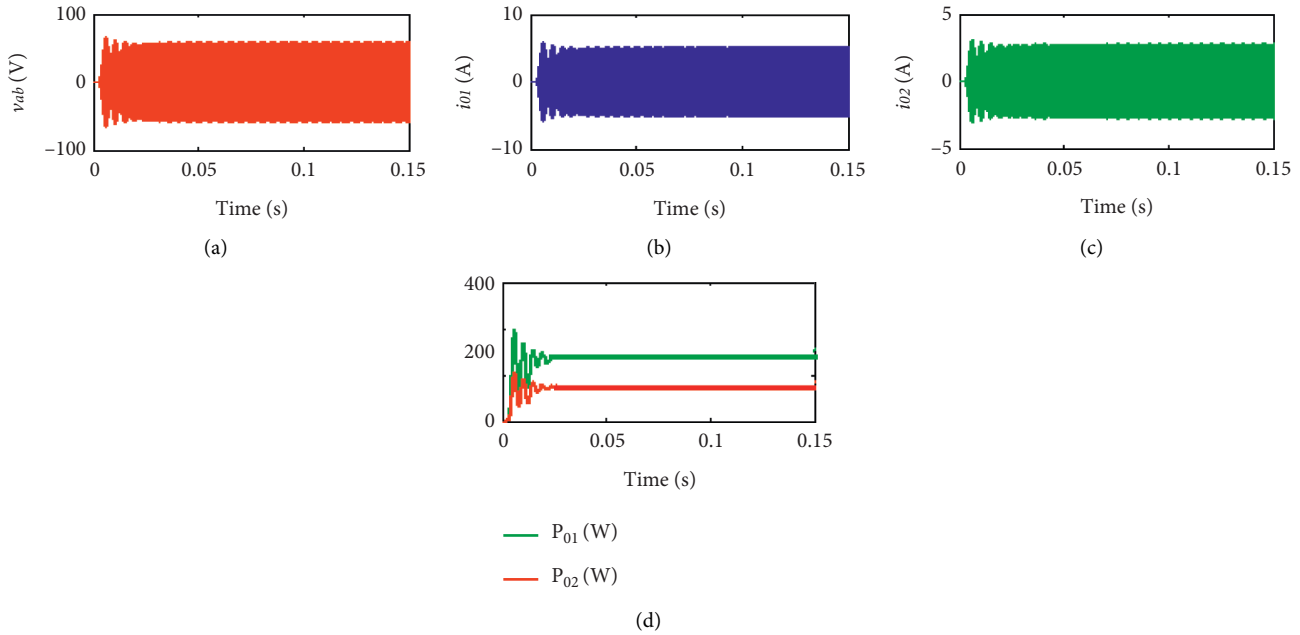

Figure 10: Main waveforms. (a) Output voltage, (b) output current of load 1 for 22 kHz switching frequency, (c) output current of load 2 for 88 kHz switching frequency, and (d) output power.

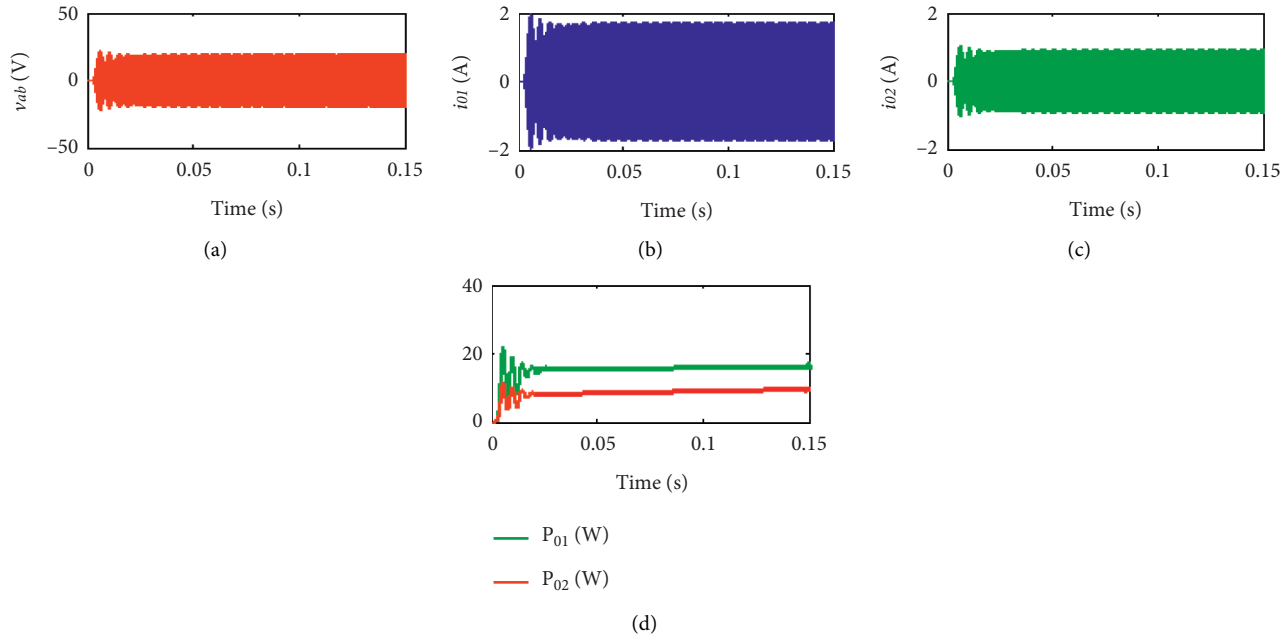

Figure 11: Main waveforms. (a) Output voltage, (b) output current of load 1 for 24 kHz switching frequency, (c) output current of load 2 for 48 kHz switching frequency, and (d) output power.

Table 4: Computation of output power.

Switching frequency (kHz)		Load 1		Load 2	
Load 1	Load 2	$I_{01(\mathrm{rms})}$ (A)	P_{01} (W)	$I_{02(\mathrm{rms})}$ (A)	P_{02} (W)
20	80	6.74	500	4.77	250
21	82	5.44	325	3.84	162.5
22	84	4.26	200	3.02	100
23	86	3.02	100	2.13	50
24	88	1.28	18	0.90	9

different switching frequencies is obtained using MATLAB/Simulink. The main waveforms for 500 W (load 1) and 250 W (load 2) output power is demonstrated in Figure 13. The output voltage waveform is shown in Figure 13(a). The output current waveform for load 1 and load 2 is illustrated in Figures 13(b) and 13(c), respectively. It is inferred from the figure that the system possesses a better response in terms of peak overshoot (% M_{p}), rise time (t_{r}), peak time (t_p), settling time (t_{s}), and steady-state error (e_{ss}). The output power waveform for load 1 and load 2 is illustrated in Figure 13(d). In order to test the performance of the system, the set power is varied from 18 W for load 1 and 9 W for load 2 respectively. The main waveform is illustrated in Figure 14 and its output voltage is presented in Figure 14(a). The output current waveform for load 1 and load 2 is illustrated in Figures 14(b) and 14(c), respectively. It is inferred from the waveforms that, as the switching frequency of the system is varied, the output power also varies, which is illustrated in Figure 14(d). Though the performance of the system is better when compared with an open-loop system, it is stable only for a 20 kHz switching frequency with an oscillation in the output waveforms. Hence, the values of controller gains need to be optimized to make the system stable with less time domain specifications.

4.3. Closed-Loop Response of SRI with Optimized PI Compensator. Any practical real-time system should be stable with lesser time-domain specifications. Hence, the values of controller gain are optimized using the Floquet stability criterion, and the values of k_p and k_i are chosen as 0.004 and 4, respectively. The output waveform forms for 500 W (load 1) and 250 W (load 2) is illustrated in Figure 15. The output voltage waveform is illustrated in Figure 15(a), and loads 1 current, load 2 current, and output power are illustrated in Figures 15(b)–15(d), respectively. It is observed that the system possesses a good dynamic behaviour, and also it is evident from Figure 7 that the system is stable. In

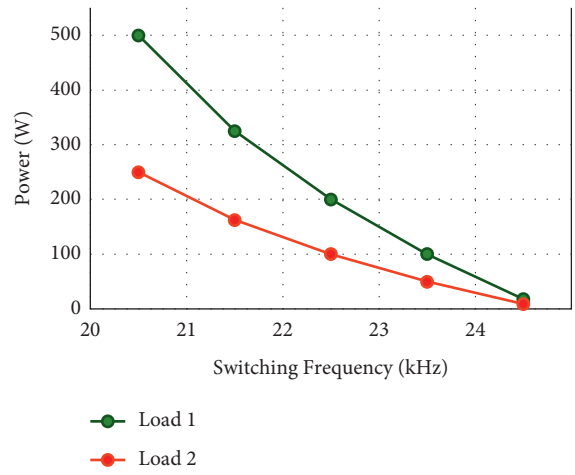

Figure 12: The impact of output power on the switching frequency variations.

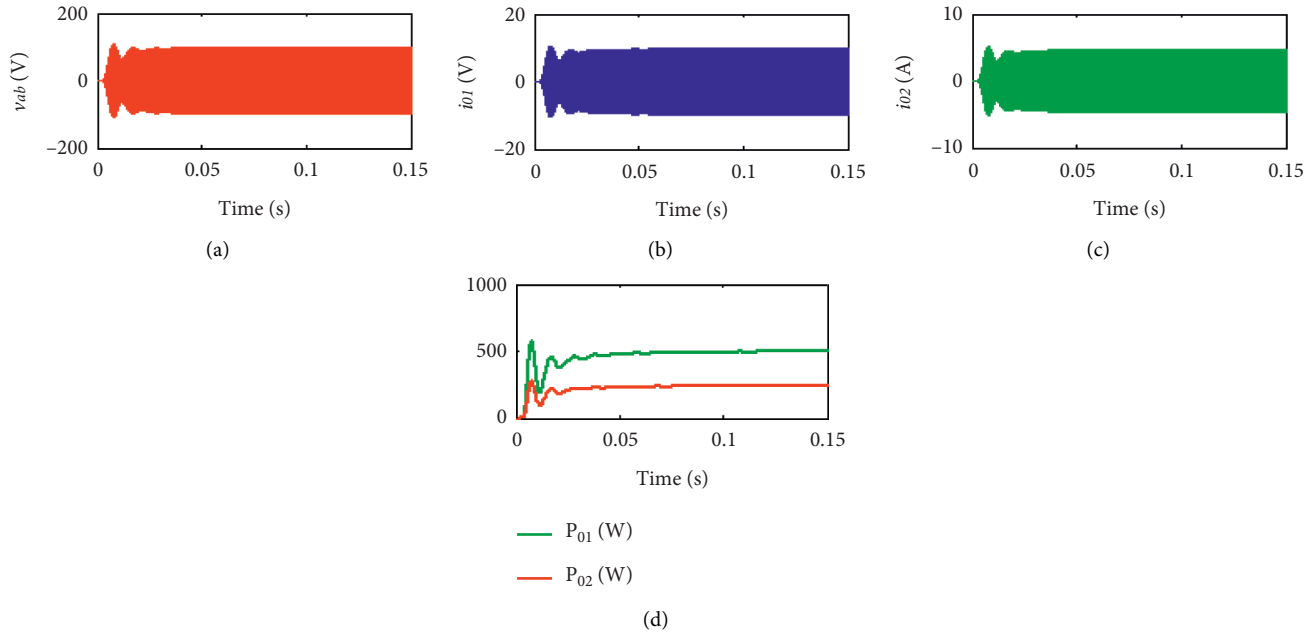

Figure 13: Main waveforms. (a) Output voltage, (b) output current of load 1 for 500 W set power, (c) output current, and (d) output power of load 2 for 250 W set power.

order to validate the performance of the proposed controller, the set power is adjusted from 500 W to 18 W in load 1 and 250 W to 9 W in load 2. The corresponding output voltage, load 1 current, load 2 current, and power waveform is illustrated in Figure 16, and the time domain response of the system is included in Table 5. It is observed that the output response of the system is better at this set power and it is also inferred that the optimized PI compensated system has a better response in terms of t_r, t_p, t_s, $\%M_p$ and e_{ss}.

5. Hardware Results of the Developed System

The validation of the proposed converter with the control algorithm is being performed using the PIC16F877A. The output pulses are amplified using a TLP250 driver IC. The HB inverter is developed with two H20R1203 IGBTs. The load current is measured using a SIGLENT CP4060 current probe and waveforms are recorded using an MDO3024 optical oscilloscope. The temperature rise in the load is studied using the FLIR E75 24° a thermal imager. The photograph of the dual-frequency HB SRI is shown in Figure 17.

From the analysis and simulation study, it is noted that the developed system is stable for the optimized values of k_p and k_i. Hence, the prototype is developed with these optimized values for the set power of 500 W (load 1) and 250 W (load 2). The output voltage and current waveforms are illustrated in Figure 18(a). The expanded view of the output voltage and current waveforms of load 1 and load 2 is

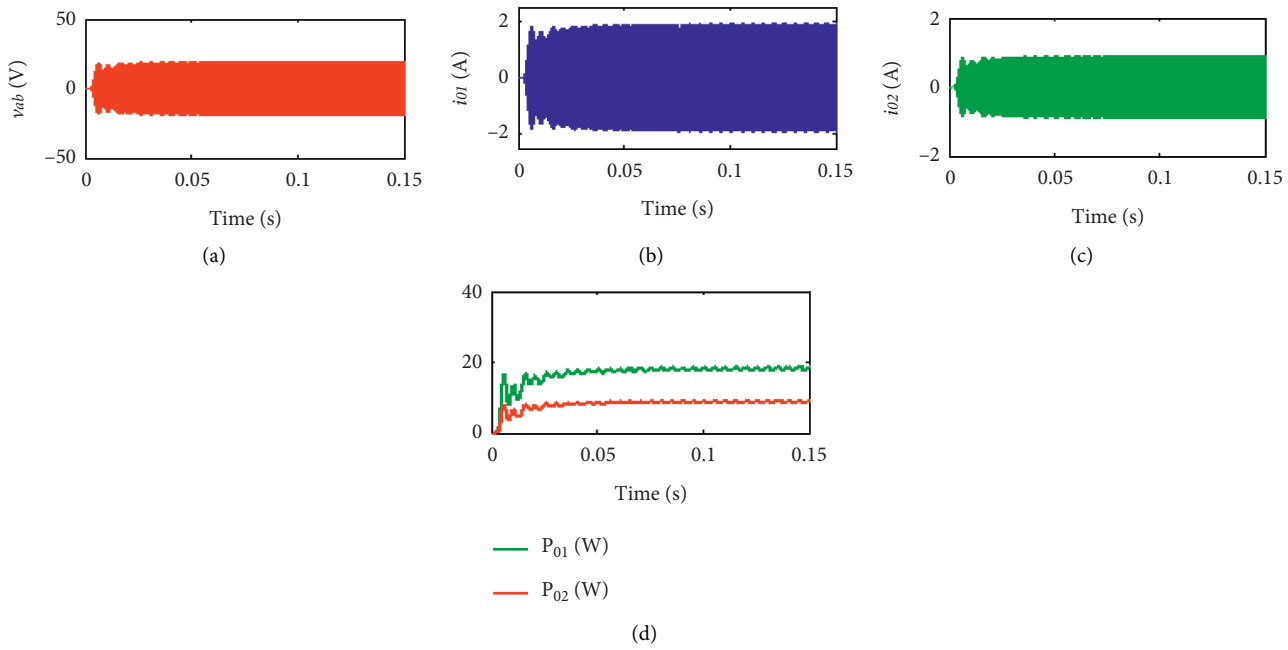

Figure 14: Main waveforms. (a) Output voltage, (b) output current of load 1 for 18 W set power, (c) output current, and (d) output power of load 2 for 9 W set power.

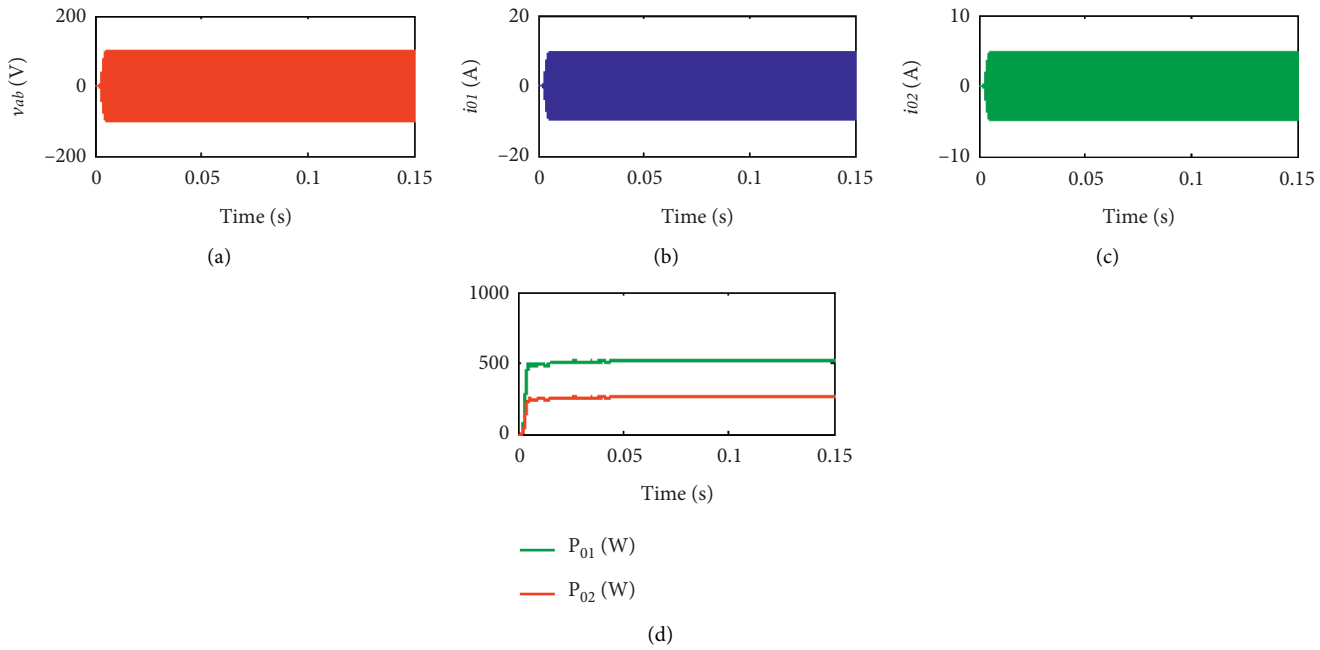

Figure 15: Main waveforms. (a) Output voltage, (b) output current of load 1 for 500 W set power, (c) output current, and (d) output power of load 2 for 250 W set power.

illustrated in Figures 18(b) and 18(c), respectively. Similarly, output voltage and current waveforms for 50 W (load 1) and 25 W (load 2) output power are shown in Figure 19. It is inferred from the figure that the output has a smooth response and also the simulation and hardware results are in line with each other.

The temperature study is carried out in the COMSOL Multiphysics software. FEM simulation is analyzed using heat transfer and magnetic field solvers by providing current, switching frequency, and load properties as the input. The system geometry has meshed with 20134 triangular elements. The contour plot of load 1 and load 2 is shown in

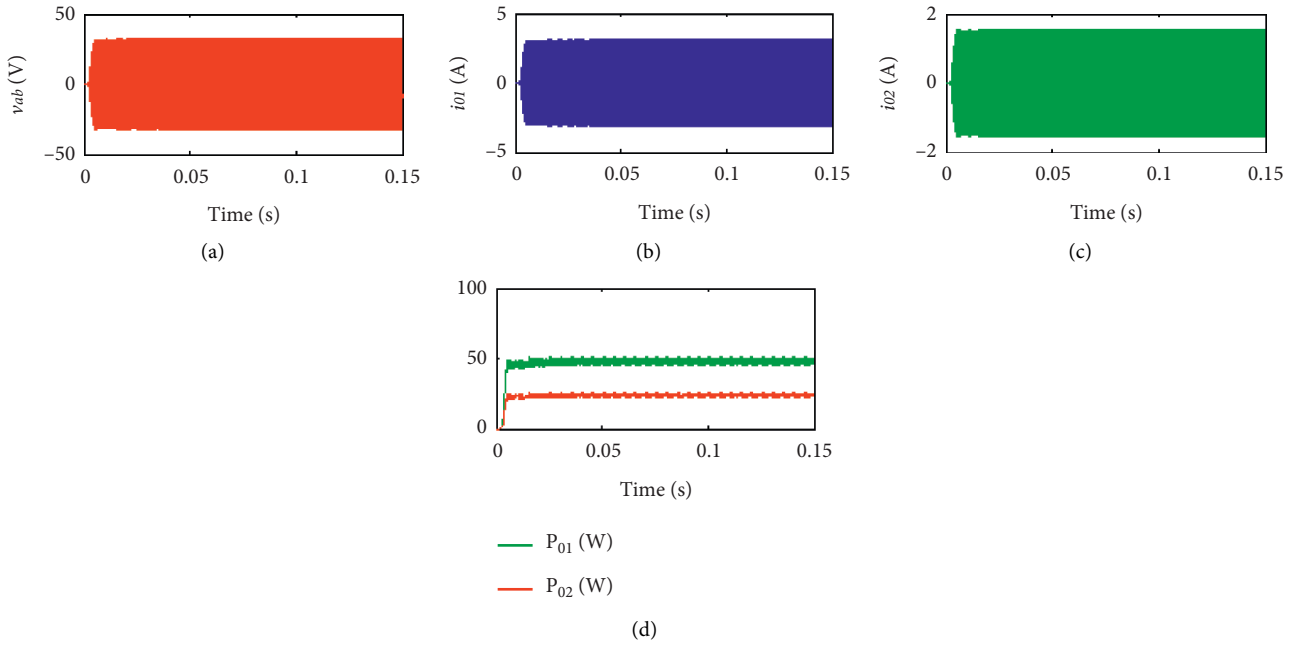

Figure 16: Main waveforms. (a) Output voltage, (b) output current of load 1 for 50 W set power, (c) output current, and (d) output power of load 2 for 25 W set power.

Table 5: Time domain response of the system.

Specifications	t_r (s)	t_s (s)	% M_p	e_{ss}
Open-loop system	0.005	0.05	80	—
PI compensated system	0.003	0.015	40	10 W (load 1) 5 W (load 2)
Optimised PI compensated system	0.0085	0.0001	0.1	0.01 W (load 1) 0.005 W (load 2)

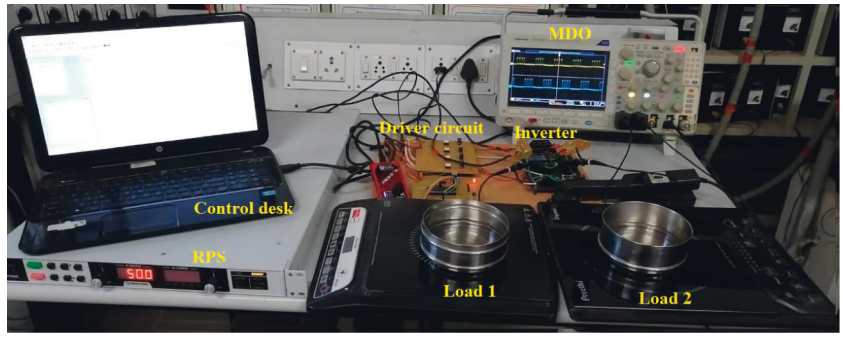

Figure 17: Photograph of the dual-frequency HB SRI.

Figures 20(a) and 20(b), respectively. The temperature distribution is evident from the plot. The experimental temperature plot is illustrated in Figure 20(c). The thermal rise is taken at the period $t = 160$ s for both loads. The maximum temperature observed was 77°C on in both the loads. An efficient comparison of the systems is illustrated in Figure 21.

5.1. The Main Achievement of the Research Work. The following points are distinctive concerning the stability analysis of the dual-frequency half-bridge inverter with variable frequency control:

(i) Output power is controlled from 90% to 10% of the rated power.

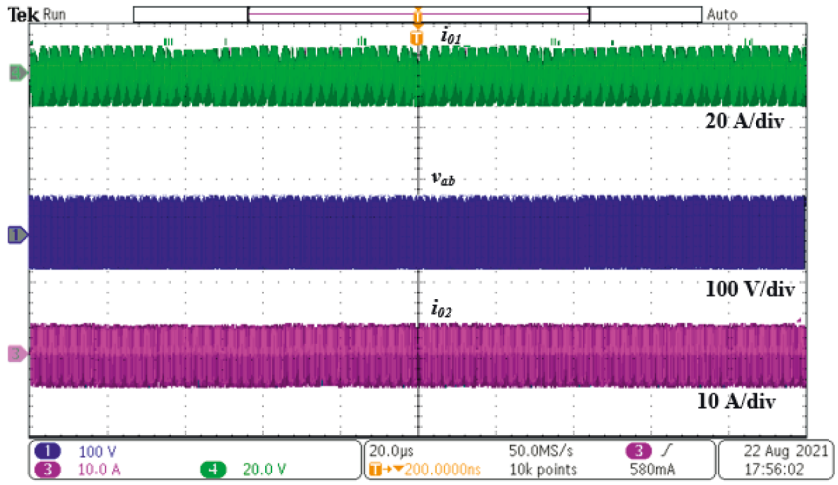

(a)

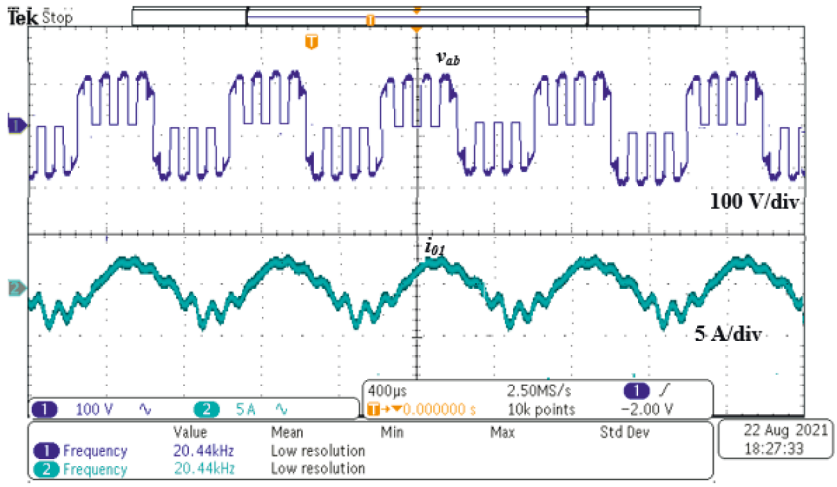

(b)

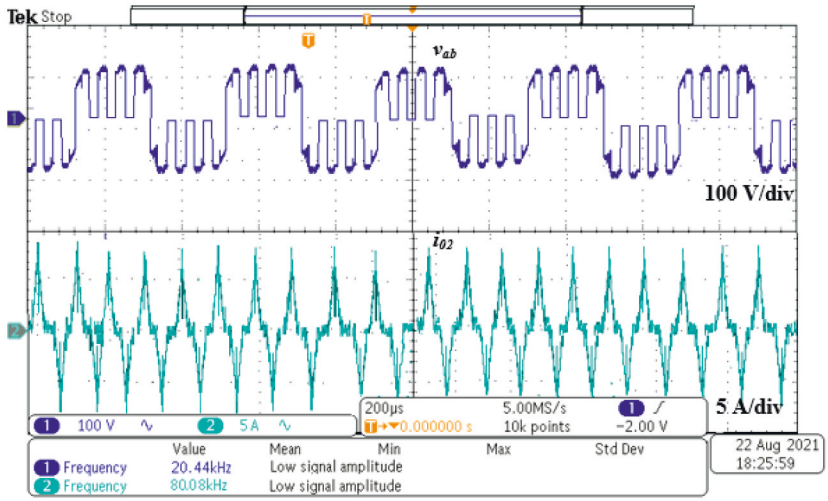

(c)

Figure 18: Main hardware waveforms for the power of 500 W (load 1) and 250 W (load 2). (a) Output voltage and current waveforms, (b) expanded output voltage and current waveforms of load 1, and (c) expanded output voltage and current waveforms of load 2.

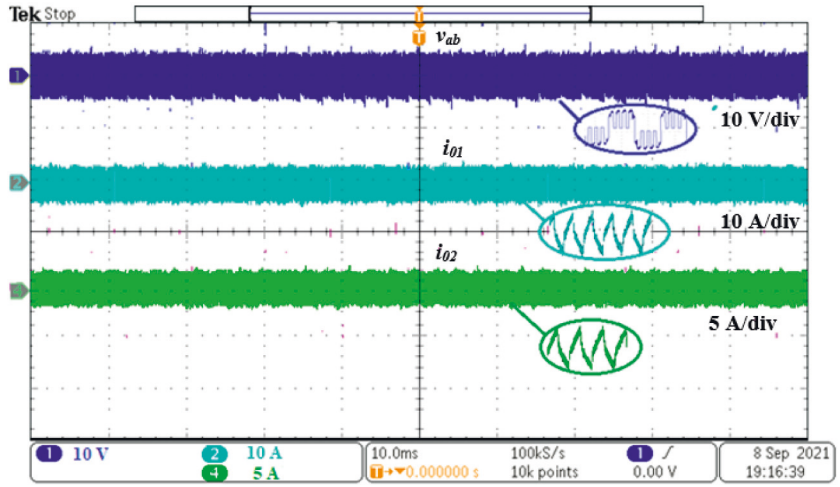

Figure 19: Main hardware voltage and current waveforms for 50 W (load 1) and 25 W (load 2) output power.

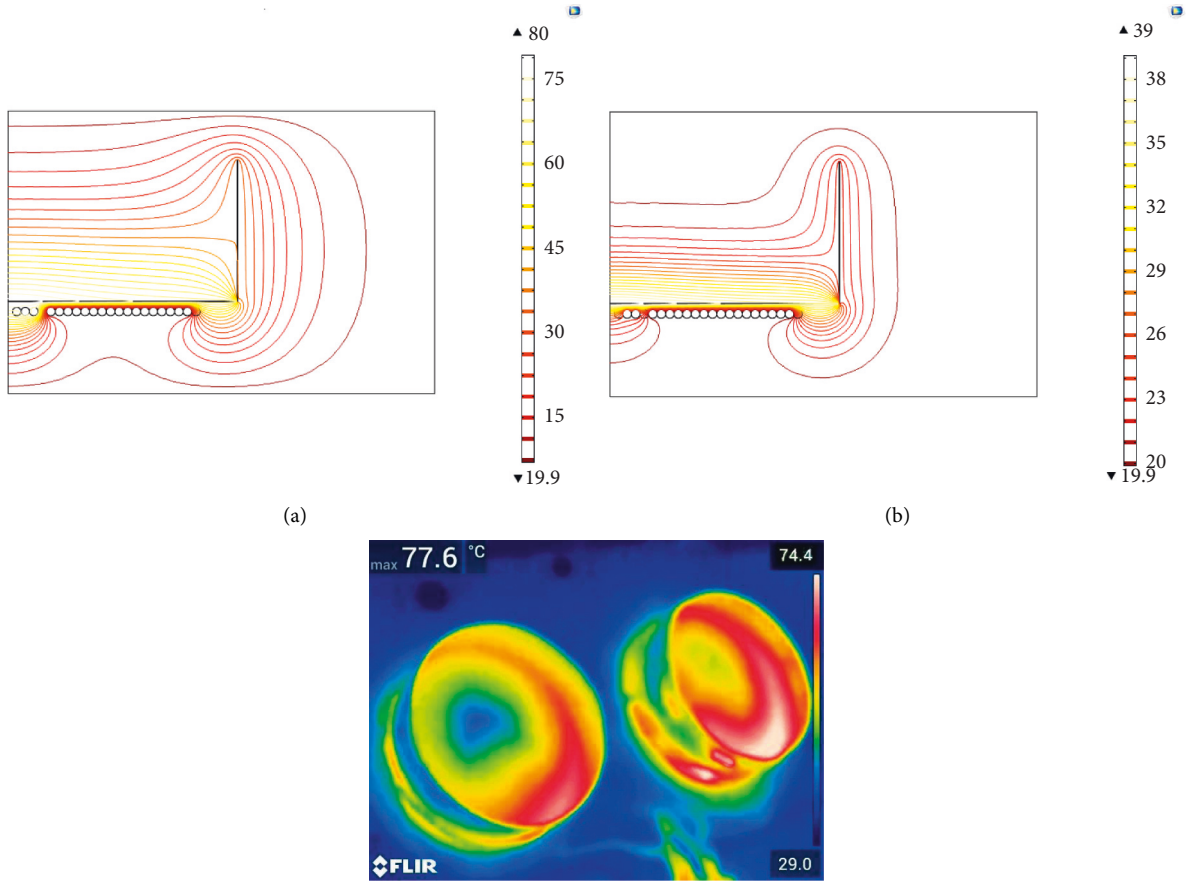

Figure 20: Thermal image. (a) Contour plot of load 1, (b) contour plot of load 2, and (c) experimental.

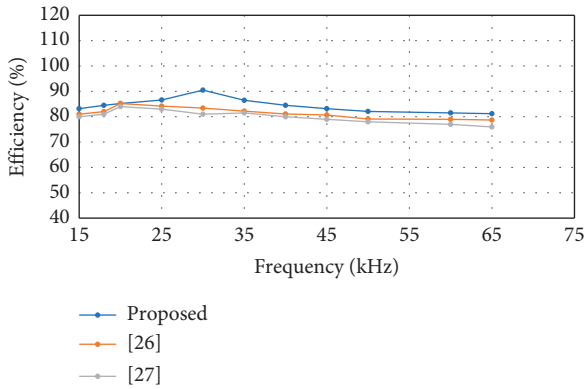

Figure 21: Efficiency comparison of the system.

(ii) The proposed inverter processes at a higher efficiency of 90.5% at the resonant frequency.

(iii) The output power is controlled independently.

(iv) The frequency of the inverter is varied to control the output power.

6. Conclusion

In this work, stability analysis of the converter is carried out based on the Floquet theory with the small-signal model of the inverter. The behaviour of the system is studied in open loop and closed loop using a PI compensator. It is found that the system becomes unstable when the switching frequency is varied. Hence, the values of controller gain are optimized using the Floquet theory to get a stable system with a better time domain response. The stability analysis is carried out for the system with the frequency variation of 20 kHz to 24 kHz for load 1 with the power variation of 500 W to 18 W and with a frequency variation of 80 kHz to 88 kHz for load 2 with a power variation of 250 W to 9 W. It is noted from the output response that the rise time is 0.0085 s, the peak time is 0.0001 s, and peak overshoot is 0.1% with minimum steady-state error. The optimized compensated system possesses better dynamic response as compared to the open-loop system and compensated system. The temperature distribution on the load is studied using FEM software and captured in real time using a FLIR thermal imager.

Data Availability

No data were used to support this study.

Conflicts of Interest

The authors declare that they have no conflicts of interest.

Authors' Contributions

Belqasem Aljafari conceptualized the study, designed the methodology, wrote the original draft, provided the resources, and performed software analysis. Pradeep Vishnu Ram validated the study, performed the formal analysis, investigation, and visualization, and reviewed and edited the manuscript. Suresh Kumar Alagarsamy reviewed and edited the manuscript and performed the software analysis. Hassan Haes Alhelou supervised the study and administered the project.

Acknowledgments

The authors are thankful to the Deanship of Scientific Research at Najran University for funding this work under the Research Groups Funding program grant code (NU/RG/SERC/11/6).

References

[1] P. Vishnuram, G. Ramachandiran, S. Ramasamy, and S. Dayalan, "A comprehensive overview of power converter topologies for induction heating applications," *International Transactions on Electrical Energy Systems*, vol. 30, no. 10, Article ID e12554, 2020.

[2] M. G. Lozinskii, *Industrial Applications of Induction Heating*, CRC Press, Boca Raton, FL, USA, 1969.

[3] J. Acero, J. M. Burdio, L. A. Barragan et al., "Domestic induction appliances: an overview of recent research," *IEEE Industry Applications Magazine*, vol. 16, no. 2, pp. 39–47, 2010.

[4] O. Lucía, P. Maussion, E. J. Dede, and J. M. Burdío, "Induction heating technology and its applications: past developments, current technology, and future challenges," *IEEE Transactions on Industrial Electronics*, vol. 61, no. 5, pp. 2509–2520, 2014.

[5] B. Saha and R. Y. Kim, "High power density series resonant inverter using an auxiliary switched capacitor cell for induction heating applications," *IEEE Transactions on Power Electronics*, vol. 29, no. 4, pp. 1909–1918, 2014.

[6] O. Lucía, J. M. Burdío, I. Millán, J. Acero, and L. A. Barragán, "Efficiency oriented design of ZVS half-bridge series resonant inverter with variable frequency duty cycle control," *IEEE Transactions on Power Electronics*, vol. 25, no. 7, pp. 1671–1674, 2010.

[7] H. W. Koertzent, J. Wyk, and J. A. Ferreira, "Design of the half-bridge, series resonant converter for induction cooking," in *Proceedings of the IEEE PESC*, pp. 729–735, Atlanta, GA, USA, June 1995.

[8] C. Bi, H. Lu, K. Jia, J. g Hu, and H. Li, "A novel multiple-frequency resonant inverter for induction heating applications," *IEEE Transactions on Power Electronics*, vol. 31, p. 1, 2016.

[9] J. M. Burdío, F. Monterde, J. R. García, L. A. Barragán, and A. Martínez, "A two-output series-resonant inverter for induction-heating cooking appliances," *IEEE Transactions on Power Electronics*, vol. 20, no. 4, pp. 815–822, 2005.

[10] F. Forest, E. Labouré, F. Costa, and J. Y. Gaspard, "Principle of a multiload/single converter system for low power induction heating," *IEEE Transactions on Power Electronics*, vol. 15, no. 2, pp. 223–230, 2000.

[11] Ó. Lucía, J. M. Burdío, L. A. Barragán, J. Acero, and I. Millán, "Series-resonant multiinverter for multiple induction heaters," *IEEE Transactions on Power Electronics*, vol. 25, no. 11, pp. 2860–2868, 2010.

[12] P. Sharath Kumar, V. Neti, and B. K. Murthy, "Dual frequency inverter configuration for multiple-load induction cooking application," *IET Power Electronics*, vol. 8, no. 4, pp. 591–601, 2015.

[13] P. Vishnuram and G. Ramachandiran, "A simple multi-frequency multiload independent power control using pulse density modulation scheme for cooking applications," *International Transactions on Electrical Energy Systems*, vol. 31, no. 3, Article ID e12771, 2021.

[14] S. Okudaira and K. Matsuse, "Adjustable frequency quasi-resonant inverter circuits having short-circuit switch across resonant capacitor," *IEEE Transactions on Power Electronics*, vol. 23, no. 4, pp. 1830–1838, July 2008.

[15] N. Booma, R. R. Sathi, and P. Vishnuram, "Fuzzy logic based voltage control scheme for improvement in dynamic response of the class D inverter based high frequency induction heating system," *Turkish Journal of Electrical Engineering and Computer Sciences*, vol. 24, pp. 2556–2574, 2016.

[16] Y. Hsieh and F. C. Lee, "Modeling resonant converters in a rotating coordinate," in *Proceedings of the 2017 IEEE Energy Conversion Congress and Exposition (ECCE)*, pp. 237–243, Cincinnati, OH, USA, October 2017.

[17] Y. Hsieh and F. C. Lee, "Modeling resonant converters in a rotating polar coordinate," in *Proceedings of the 2018 IEEE Applied Power Electronics Conference and Exposition (APEC)*, pp. 938–943, San Antonio, TX, USA, March 2018.

[18] A. Domínguez, L. A. Barragán, A. Otín, J. I. Artigas, I. Urriza, and D. Navarro, "Small-signal model of dual half-bridge series resonant inverter sharing resonant capacitor for domestic induction heating," in *Proceedings of the IECON 2014-40th Annual Conference of the IEEE Industrial Electronics Society*, pp. 3277–3282, Dallas, TX, USA, October 2014.

[19] P. Vishnuram, S. Ramasamy, P. Suresh, and A. Sureshkumar, "Phase-locked loop-based asymmetric voltage cancellation for the power control in dual half-bridge series resonant inverter sharing common capacitor for induction heating applications," *Journal of Control, Automation and Electrical Systems*, vol. 30, no. 6, pp. 1094–1106, 2019.

[20] J. Zhang, *Stability Bifurcation Theory and Applications of Nonlinear Dynamical Systems*, Xi'an Jiaotong University Press, Xian, China, 2010.

[21] J. Bian, L. Hong, and T. Q. Zheng, "Stability analysis of grid-connected inverters with LCL-filter based on harmonic balance and floquet theory," in *Proceedings of the Power Electronics Conference (IPEC-Hiroshima 2014-ECCE-ASIA) 2014 International*, pp. 3314–3319, Hiroshima, Japan, May 2014.

[22] H. Li, J. Shang, X. You, T. Zheng, B. Zhang, and J. Lü, "A novel stability analysis method based on floquet theory for cascaded DC-DC converters system," in *Proceedings of the 2015 IEEE Energy Conversion Congress and Exposition (ECCE)*, pp. 2679–2683, Montreal, Canada, September 2015.

[23] H. Li, Z. Guo, F. Ren, X. Zhang, and B. Zhang, "A stability analysis method based on Floquet theory for multi-stage DC-DC converters system," in *Proceedings of the 2017 IEEE Energy Conversion Congress and Exposition (ECCE)*, pp. 3025–3029, Cincinnati, OH, USA, October 2017.

[24] G. Floquet, "Sur les équations différentielles linéaires à coefficients périodiques," *Annales scientifiques de l'École Normale Supérieure, Série 2, Tome*, vol. 12, pp. 47–88, 1883.

[25] H. Li, Y. Zou, X. Jiang, and C. Liu, "A time-domain stability analysis method for LLC resonant converter based on Floquet theory," *Microelectronics Reliability*, vol. 114, Article ID 113850, 2020.

[26] P. Vishnuram and G. Ramachandiran, "Capacitor-less induction heating system with self-resonant bifilar coil," *International Journal of Circuit Theory and Applications*, vol. 48, no. 9, pp. 1411–1425, 2020.

[27] A. Sureshkumar, R. Gunabalan, P. Vishnuram, S. Ramsamy, and B. Nastasi, "Investigation on performance of various power control strategies with bifilar coil for induction surface melting application," *Energies*, vol. 15, no. 9, p. 3301, 2022.